STRUCTURAL BIOLOGY

Chiral switching in biomineral suprastructures induced by homochiral L-amino acid

Wenge Jiang[1], Michael S. Pacella[2], Hojatollah Vali[3], Jeffrey J. Gray[4,5], Marc D. McKee[1,3]*

How homochiral L-biomolecules in nature induce a chiral switch in biomineralized architectures is unknown, although chiral switching is common in many calcium carbonate–hardened structures found in marine and terrestrial organisms. We created hierarchically organized, chiral biomineral structures of calcium carbonate, whose chirality can be switched by a single L-enantiomer of an amino acid. The control of this chiral switching involves two stages: a calcium carbonate (vaterite) platelet layer inclination stage, followed by a platelet layer rotation stage, the latter stage being responsible for successional chiral switching events within the biomineralized structures. The morphology of the synthesized chiral vaterite structures remarkably resembles pathologic chiral vaterite otoconia found in the human inner ear. In general, these findings describe how a single-enantiomer amino acid might contribute to biomineral architectures having more than one chirality as is commonly seen in biology, and more specifically, they suggest how pathologic chiral malformations may arise in humans.

INTRODUCTION

Chirality—one of the most striking features of the living world—exists at all levels in biology, from single amino acid molecules to the long macroscopically helical tooth of the narwhal. Specifically pertaining to calcium carbonate biominerals that record Earth's transition from an inorganic to a biologic world (1), chiral switching is common and can be found in many hardened structures of terrestrial and marine organisms. In terrestrial spiraling gastropod shells for example, changes in chirality can frequently be found not only in different species but also within the same species, even within one shell's different parts (2–6). Similarly, in marine biology, chiral switching phenomena range from the microlevel to the macroscale, notably in the spiraling skeletons of marine foraminifera and in hierarchically organized coccolith skeletons (7–11). Even more of interest, at the microscale level in coccolith organization, circular layers (cycles) of calcium carbonate can have different subunit configurations, where two adjacent layers can have opposite clockwise and counterclockwise orientations, thus showing that different chiralities can even coexist within a single coccolith skeleton (Fig. 1A) (9–11). These examples of chiral switching in biomineralization are indeed remarkable and must be controlled by a strategic switching process that results in precise hierarchical organization.

At the molecular level, predominant thinking supposes that the different handedness of chiral structures of calcium carbonate biominerals in principle results from the effects of different chiral forms of molecules, that is, L- and D-enantiomers (7, 12–15). Enantiomeric pairs of L- and D-molecules (each having the opposite configuration of the other), which includes amino acids, peptides, and proteins, can induce in the laboratory setting enantiomeric (chiral) calcium carbonate mineral suprastructures having opposite orientations (7, 16–19). However, in nature, this cannot be the case, where biologic homochirality exists such that only L-amino acids and L-biomolecules

are involved in biological processes—except for a few rare cases such as in deep sea bacteria where D-forms are used (20, 21). Thus, the notion that the actions of enantiomeric pairs of L-and D-molecules can lead to chiral switching during biomineral formation, where opposite enantiomorphs of biomineral appear, is invalid. The mechanism by which only single chiral L-biomolecules can create the common phenomenon of chiral switching in biominerals remains unknown.

The acidic amino acid aspartic acid (Asp)—an abundant component of biomineralization-regulating proteins (22)—is thought to play a particularly significant role in biomineralization, particularly in coccolith skeletons (23), otoconia and otoliths (24–26), and in the origin of homochiral biomolecules (21, 27, 28). Here, we have synthesized with solution chemistry and the single L-enantiomer form of Asp, chiral and hierarchically organized suprastructures of calcium carbonate vaterite (toroids/helicoids) that are created through a chiral switching mechanism. This heretofore undescribed chiral switching model regulated by a single enantiomer (L-Asp) might provide insight for common chiral switching phenomenon observed in biomineralized structures found in biology.

Surprisingly, the synthesized chiral vaterite structures that we have produced in the laboratory setting remarkably resemble pathologic chiral vaterite otoconia found in the human inner ear (Fig. 1, B and C), structures which normally function in the vestibular apparatus to maintain balance by gravity sensing and by detecting linear acceleration (29). Vaterite is a polymorph of calcium carbonate sometimes associated with pathologically calcified tissues in humans including in gallstones (30), pancreatic stones, and calcified heart valves (31), and vaterite is also found in chiral-hardened structures of terrestrial and marine organisms such as in regenerated (after damage) helical gastropod shells and in the spiral skeletons of the solitary stolidobranch ascidian *Herdmania momus* and planktic foraminifera (32–34). Otoconia can show abnormal, pathologic rounded chiral vaterite (29), when normally they are symmetric calcitic structures with straight edges, angles, and large crystal facets. In a report on pathologic otoconia observed in an aged patient, the rounded overall chiral morphology of these abnormal structures consisted of assembled vaterite platelet subunits (Fig. 1B), with evidence suggesting they originated from a precursor achiral flat vaterite disc (29, 35). The consequences of this otoconial pathology could include impairment or loss of balance,

[1]Faculty of Dentistry, McGill University, Montreal, Quebec H3A 0C7, Canada. [2]Department of Biomedical Engineering, Johns Hopkins University, Baltimore, MD 21218 USA. [3]Department of Anatomy and Cell Biology, Faculty of Medicine, McGill University, Montreal, Quebec H3A 0C7, Canada. [4]Department of Chemical and Biomolecular Engineering, Johns Hopkins University, Baltimore, MD 21218, USA. [5]Program in Molecular Biophysics, John Hopkins University, Baltimore, MD 21218, USA.
*Corresponding author. Email: marc.mckee@mcgill.ca
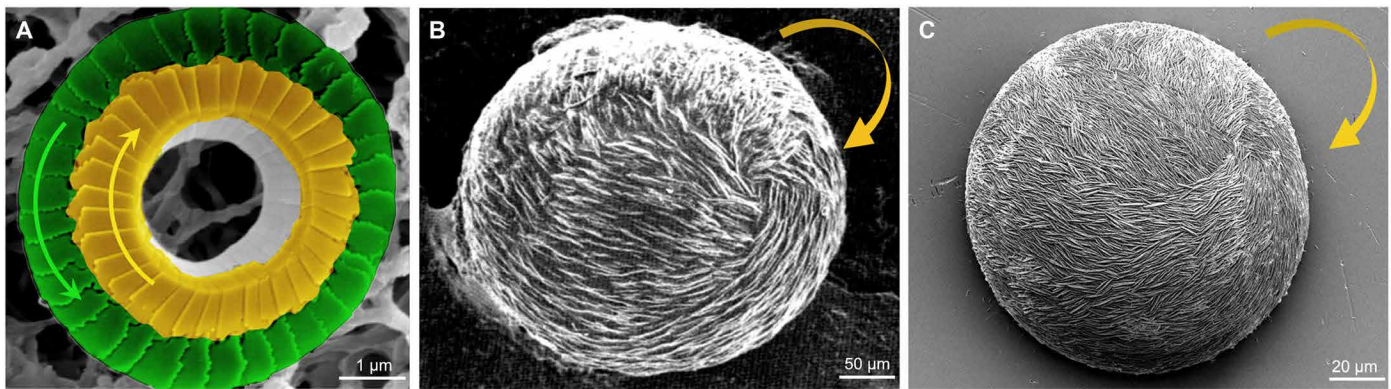
Fig. 1. Hierarchically organized chiral biomineralized architectures constructed of calcium carbonate. (**A**) Scanning electron microscopy (SEM) image showing coexistence of adjacent imbricated, calcitic coccolith skeletal-plate layers (cycles) oriented in the clockwise direction centrally (yellow) and in the counterclockwise direction peripherally (green) in *Umbilicosphaera foliosa* [reprinted with permission from (*9*)]. (**B**) Rounded, chiral (clockwise, yellow arrow) pathologic calcium carbonate vaterite otoconia from the inner ear of an aged patient [reprinted with permission from (*29*)]. (**C**) Synthetic chiral (clockwise, yellow arrow) suprastructure of hierarchically organized vaterite induced by the amino acid ʟ-Asp as prepared in a laboratory setting.

severe vertigo and nausea, and/or susceptibility to balance-related falls, which is the leading cause of accidental bone fracture and death in the elderly population (*24*, *36*). To date, unlike what is known for the extensively investigated normal and symmetric faceted calcium carbonate otoconia (*24*, *25*), little is known about the mechanisms that create the rounded pathologic chiral vaterite form. Beyond describing implications for chirality in biomineralization processes in general, our work also predicts how pathologic chiral malformations might arise in human otoconia.

RESULTS AND DISCUSSION
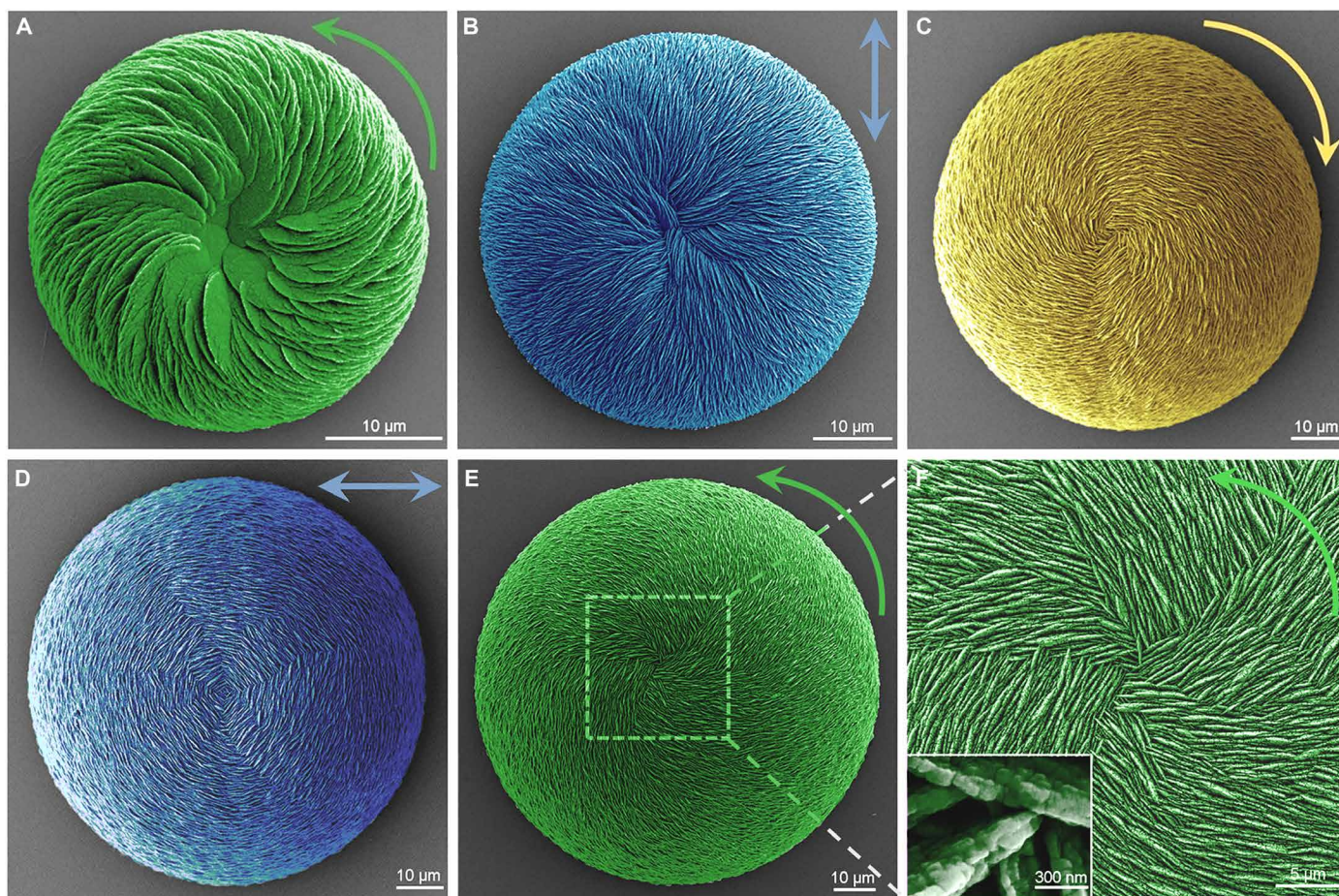### Switching the chirality of vaterite suprastructures
In the absence of any amino acid additive, supersaturated calcium- and carbonate-containing solutions predominantly produce characteristic rhombohedral calcite crystals (the most thermodynamically stable phase of $CaCO_3$), but also occasionally yield achiral vaterite crystals having hexagonal symmetry; the latter are thermodynamically unstable and, with time, dissolve and transform to calcite (fig. S1). However, when the chiral acidic amino acid Asp is added to the growth solution, vaterite forms as the predominant mineral phase; this phase is stable over a growth evolution process ranging from the microlevel to the visible submillimeter level occurring for as long as a year or more, which allows investigation of hierarchical growth of vaterite structures over long periods of time. During this time, we observed by SEM that vaterite grown in the presence of a single enantiomer of Asp, over a time period of months, demonstrated chiral switching (Fig. 2 and fig. S2).

In the presence of the single ʟ-enantiomer of Asp, small vaterite helicoid-shaped suprastructures with subunit inclination and spiraling curved chiral platelets oriented in the right-handed direction (Fig. 2A, counterclockwise green arrow) formed at the initial stage—the chirality resulting from nanoparticle (nanohexagonal prisms) counterclockwise tilting after binding of ʟ-Asp to their surfaces (Fig. 2A, green) (*19*). However, with further growth developing this initial chiral morphology, the vaterite helicoids enlarged, the counterclockwise chirality disappeared, and transitional achiral vaterite helicoids appeared having a straight-radiating (relative to the centroid of the helicoid) vertical platelet orientation (Fig. 2B, blue). With

additional time, chiral switching to the clockwise direction was noted in the larger helicoids, where vertical chiral platelets now grew with a left-handed orientation (Fig. 2C, yellow). With even more time, an achiral transitional helicoidal form reappeared showing horizontal-surrounding (relative to the centroid of the helicoid) vertical platelet orientation (Fig. 2D, blue). Finally, with even more time, large right-handed counterclockwise vaterite helicoids were then observed (Fig. 2E, green), where coiled and aligned vertical platelets radiated from the centroid of the suprastructure (Fig. 2F). All vaterite platelets were nanostructured, with nanoparticles being roughly 20 nm in size as measured by high-resolution SEM, a feature we described in detail previously (*19*). Here, similar to the results obtained using the ʟ-Asp enantiomer, use of ᴅ-Asp reproduced all the same chiral switching processes of vaterite helicoid growth but with the completely opposite directions; from the clockwise direction initially to transitional achiral straight-radiating platelets, and then switching to the counterclockwise direction at an intermediate stage, and then to the achiral horizontal-surrounding platelet orientation, and finally back to the clockwise direction (figs. S2 and S3). Thus, without any change in temperature, pH, or stirring, exposure to a single chiral enantiomer of acidic amino acid in solution was sufficient to induce chiral switching over time during the growth evolution of these hierarchically organized vaterite suprastructures.

Coexistence of vaterite helicoid enantiomorphs
Inspired by the known coexistence of various enantiomorphs of biominerals in nature, such as the right- and left-handedness of chiral marine coccolith suprastructures and terrestrial snail shell, we next examined whether different chiral enantiomorphs of vaterite helicoids could coexist (in the same closed system) in the presence of a single ʟ-amino acid enantiomer. This was the case in the presence of the single-enantiomer ʟ-Asp, where high supersaturation conditions for calcium and carbonate ions induced nascent helicoids to be continuously nucleated at the same time as existing ones continued to grow. This process resulted in a full range of helicoid sizes (with their respective alternating chirality) demonstrating coexistence of different enantiomorphs at any given time (Fig. 3), as occurs in biology. In contrast, under low supersaturation conditions, nucleated vaterite helicoids all grew simultaneously and had uniform growth rates and

Fig. 2. Chiral switching of hierarchically organized vaterite suprastructures induced by a single chiral enantiomer of amino acid. (**A**) SEM image of an initial vaterite helicoid with right-handed (counterclockwise), inclined spiraling chirality (green) as grown in the presence of L-Asp for 24 hours. (**B**) Achiral vaterite helicoid with straight-radiating (relative to the centroid, blue) vertical vaterite platelets formed after 3 days of growth. (**C**) With time, chiral switching appears first as a left-handed (clockwise, yellow) spiraling vaterite helicoid consisting of vertical vaterite platelets after 1 week of growth. (**D**) Again, with more time (2 weeks), achiral vaterite helicoids are formed having horizontal-surrounding vertical platelet orientation (relative to the centroid, blue). (**E**) Right-handed (counterclockwise, green) vaterite helicoids are found at 1 month with interlacing vertical platelets assembled into the helicoidal suprastructure (**F**). All platelets have nanoparticle subunit structure [inset in (F)].

size for the whole growth process, with all having the same chirality (fig. S3); here, vaterite helicoid growth predominated, with no nascent vaterite helicoid nucleation (see also Supplementary Text). Thus, like the precise control that occurs in biology, we were able to precisely control the state of chiral vaterite helicoids using a single enantiomer of Asp.

Two stages of helicoid growth
To understand how a single enantiomer of an acidic amino acid could switch chirality and induce the different chiral enantiomorphs of the vaterite helicoids over time and size, we used SEM and focused-ion beam (FIB) cross sectioning to examine a time course of the evolution of the chiral switching in the presence of the single L-enantiomer of Asp (Figs. 4 and 5, and figs. S4 and S5). From these results, it was determined that the chiral switching was the result of imperfect oriented (not aligned) attachment growth mechanisms—a common strategy in nature for creating complex hierarchical materials with specific morphologies and functions such as formed by CaCO$_3$ and TiO$_2$ (1, 37–39). At both the nano- and microscale in the vaterite helicoids induced by selective adsorption of chiral acidic amino

acids on specific vaterite crystal planes (19), the evolutionary process of this chiral switch can be separated into two stages as the helicoids enlarge: (i) an initial, progressively chiral platelet layer inclination stage (relative to a basal, flat horizontal plane) which extends toward an achiral, vertical platelet organization, and (ii) a subsequent platelet layer rotation stage where successional chiral switching events occur at the surface of the helicoids.

Loss of helicoid chirality through platelet layer-by-layer inclination
In the first platelet layer inclination stage, the vaterite helicoids develop from an initial substrate core from which arise curved-edge, chiral inclined platelets (Fig. 4A). As we described previously (19), the initial chirality of a vaterite helicoid having a counterclockwise orientation induced by L-Asp comes from the nanoparticle (nanohexagon) tilting growth model. In more detail, this occurs through the adsorption of L-Asp on the vaterite (100) plane of "mother" hexagonal nanoparticles to break the perfectly oriented nucleation/attachment mechanism for the consequential "daughter" hexagonal nanoparticle. This results in a slight, misaligned counterclockwise
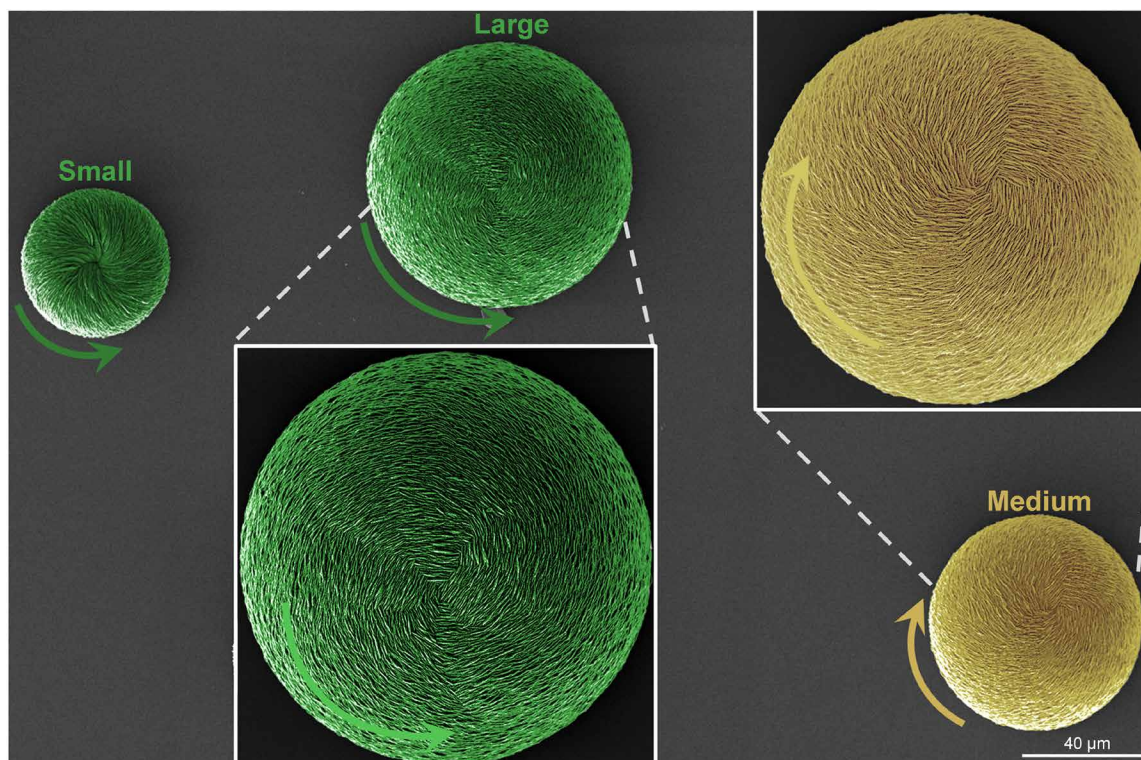
Fig. 3. Coexistence of enantiomorphs of hierarchically organized vaterite helicoids induced by a single amino acid enantiomer (L-Asp) at high supersaturation conditions. SEM images of small, counterclockwise vaterite helicoids (short green arrow) having inclined platelets, medium clockwise helicoids (yellow) having vertical platelets, and large counterclockwise helicoids (long green arrows) having vertical platelets.

tilt angle of 4° between the nanoparticles in each platelet (Fig. 4), which we terms as the nanointraplatelet tilting effect. With further replication and amplification of this tilting effect induced by L-Asp during vaterite platelet formation and extension, curved-edge, oriented counterclockwise platelets arise from the helicoid surface. With further growth of the helicoidal structure, additional counterclockwise platelets arise to generate an initial counterclockwise helicoid in the presence of L-Asp (*19*). In this platelet growth region, the platelet layers are inclined (rather than being parallel), with the inclination angle between platelet layers being about 6° as measured by FIB and high-resolution SEM (Fig. 4E). This continuous layer-by-layer inclination growth mode results in greater overall tilt angles toward the vertical; this results in a chirality decrease from the initial counterclockwise helicoid (Fig. 4, A to D). As the last step of the inclined-platelet helicoid growth mechanism, the initial counterclockwise chirality of the helicoid disappears completely when top-layer platelets (forming the 15th layer) become vertical (90°) to the original flat substrate (Fig. 4F). At this point, the helicoid presents with straight-radiating vertical platelets (Fig. 4D). During this inclined-platelet growth stage, the initially exposed basal (001) plane (light blue region) of the vaterite nanohexagons that form the chiral curved-edge platelet layers gradually decreases, and the (100) vaterite plane (dark blue region) gradually becomes increasingly exposed, as confirmed by high-resolution transmission electron microscopy (*19*). When the 15th (straight vertical) platelet layer appears as the top layer at the helicoid surface, the exposed (100) plane completely replaces the original (001) plane to become the new basal face (Fig. 4G) for further growth of the helicoid in the platelet rotation stage (see below).

Chiral switching by platelet layer-by-layer rotation

When vertical platelet orientation has been achieved at the end of the inclination stage, which involves exclusively the vaterite (100) plane for amino acid binding, the dense packing (observed by SEM) of the vertical platelets precludes further growth in this mode. As a result, new platelet growth necessarily proceeds using the exposed (100) vaterite plane of the nanoparticles/platelets; this organization triggers the second stage of helicoid growth—the vertical platelet layer rotation stage. In this case, nascent vertical platelets form as a new layer on top of the 15th vertical, straight-radiating achiral platelet layer, as a new surface layer of platelets is added, which results in an increase in the height of the helicoids (fig. S4). Important to this process is the adsorption of chiral Asp enantiomer to break the original symmetry of the newly exposed (100) vaterite plane to create a new "chiral" surface exposed to the growth solution (*19*), as has been shown for bestowing chirality to symmetric copper (110) by the adsorption of chiral tartaric acid (*40*). Consequently, for vaterite, this new chiral asymmetric configuration at the (100) interface, caused by the adsorbed chiral amino acid, does not match the symmetric lattice structure of crystalline vaterite, which leads to an altered chiral growth pattern, as has been similarly shown for ligand-induced twisting of nanoplatelets to form chiral helical ribbons of cadmium selenide (*41*, *42*). In our vaterite experiments using L-Asp, a new rotation mode begins (another imperfect oriented attachment) occurring between vertical platelet layers—the "microinterplatelet layer effect"—which is responsible for the chiral switching in the helicoid evolution process (Fig. 5). An example is illustrated here using chiral L-Asp enantiomer in the growth solution; initially, three successive clockwise vaterite
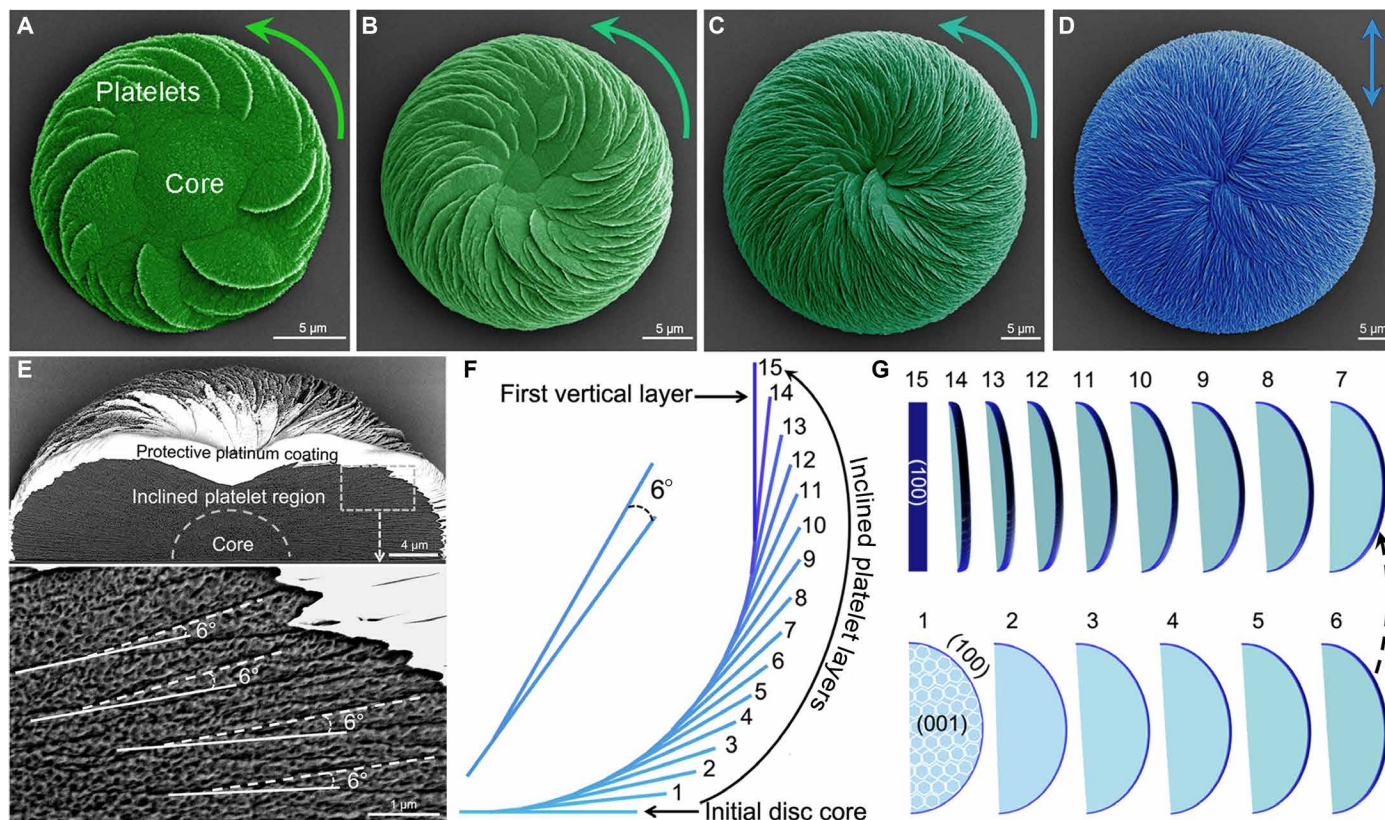
Fig. 4. Platelet layer-by-layer inclination decreases vaterite helicoid chirality toward an achiral, vertical platelet organization. (**A** to **C**) SEM images of the gradual decrease in chirality (green, pseudocolored at 8, 16, and 32 hours of growth) of vaterite helicoids grown in the presence of L-Asp. The helicoids are composed of inclined platelets originating from an initial achiral substrate disc core, growing to the point (note decreasing magnification) where the helicoid is symmetric and achiral [blue in (**D**), at 72 hours) with vertically oriented platelets at the helicoid surface, and with an increase in overall helicoid size. (**E**) SEM image of a cross section of a small intermediate counterclockwise chiral vaterite helicoid after FIB cutting, whose interior is composed of two regions—an initial core disc/dome and an inclined-platelet region (top panel). In the inclined-platelet region, the layer-by-layer growth produces inclined-platelet organization having an angle of 6° between a consequential daughter platelet layer (white dashed line on the daughter platelet) arising from a mother platelet layer (white solid line on the mother platelet), which leads to the decrease and disappearance of chirality of the vaterite helicoid as the platelets ascend to the vertical orientation. (**F**) Side view schematic of growth in the layer-by-layer inclination model where 6° inclination of 15 continuously forming platelet layers arising from an initially flat achiral core disc ascend to the first vertical platelet layer (15th dark blue line). (**G**) The exposed crystalline vaterite face changes from being initially the basal (001) vaterite plane (light blue) to the (100) plane (dark blue) after the formation of 15 successional nanostructured vaterite platelet layers, with all platelets formed from subunit tilted nanohexagons (19).

helicoids were formed (yellow arrows) with an increase in helicoid size, relative to the first straight-radiating achiral transitional helicoid (with 0° rotation; Fig. 4D). In the presence of L-Asp, there were vertical platelet successional clockwise rotations of 22.5° visible in the top layer (Fig. 5). Initially, these rotations (to reach first 22.5°, then 45°, and then 67.5° relative to the reference start point centroid at 0°) resulted in clockwise helicoid chirality (Fig. 5, A to C, small yellow bars). When the vertical platelets in the uppermost layer continued to rotate clockwise to the horizontal position (90° from the reference start point), the helicoid became achiral. This transition defined the second achiral state, where vertical platelets have a horizontal-surrounding orientation (surrounding the centroid; Fig. 5D, gray double-headed arrow and bar). With further clockwise rotational growth beyond the second transitional achiral horizontal-surrounding platelet state (to reach first 112.5°, then 135°, and then 157.5°; Fig. 5, E to G, green bars), helicoids had a counterclockwise chiral appearance. Finally with additional growth, a transitional achiral state of the helicoid (at 180°) again appeared (Fig. 5H, gray double-headed arrow, gray bar), completing a cycle to again form an achiral structure with the same

morphology as that of the original straight-radiating platelet orientation (0°) of achiral helicoids (as shown earlier in Fig. 4D), but now having a much larger size attributable to the additional growth by platelet layer additions.

Mechanism leading to chiral switching

Given the phenomenon of this chiral switching that occurs at the surface of vaterite helicoids induced by vertical platelet layer rotation between different layers, we surmised that successional layer-by-layer assembly of the helicoid structure would progress over time (and over increasing helicoid size) such that large, post-first stage helicoids would have a series of successively rotated-platelet layers, similar to the formation of layered chiral nematic structure of liquid crystals found in beetle exoskeletons and mesoporous silica films (43, 44). Beyond the initial core center and the stage 1 inclined-platelet growth region of the helicoids, this layer-by-layer assembly structure in the stage 2 rotated-platelet region was identified by SEM on cross sections of very large helicoids (fig. S5). For the transitional achiral helicoids having horizontal-surrounding vertical platelet orientation
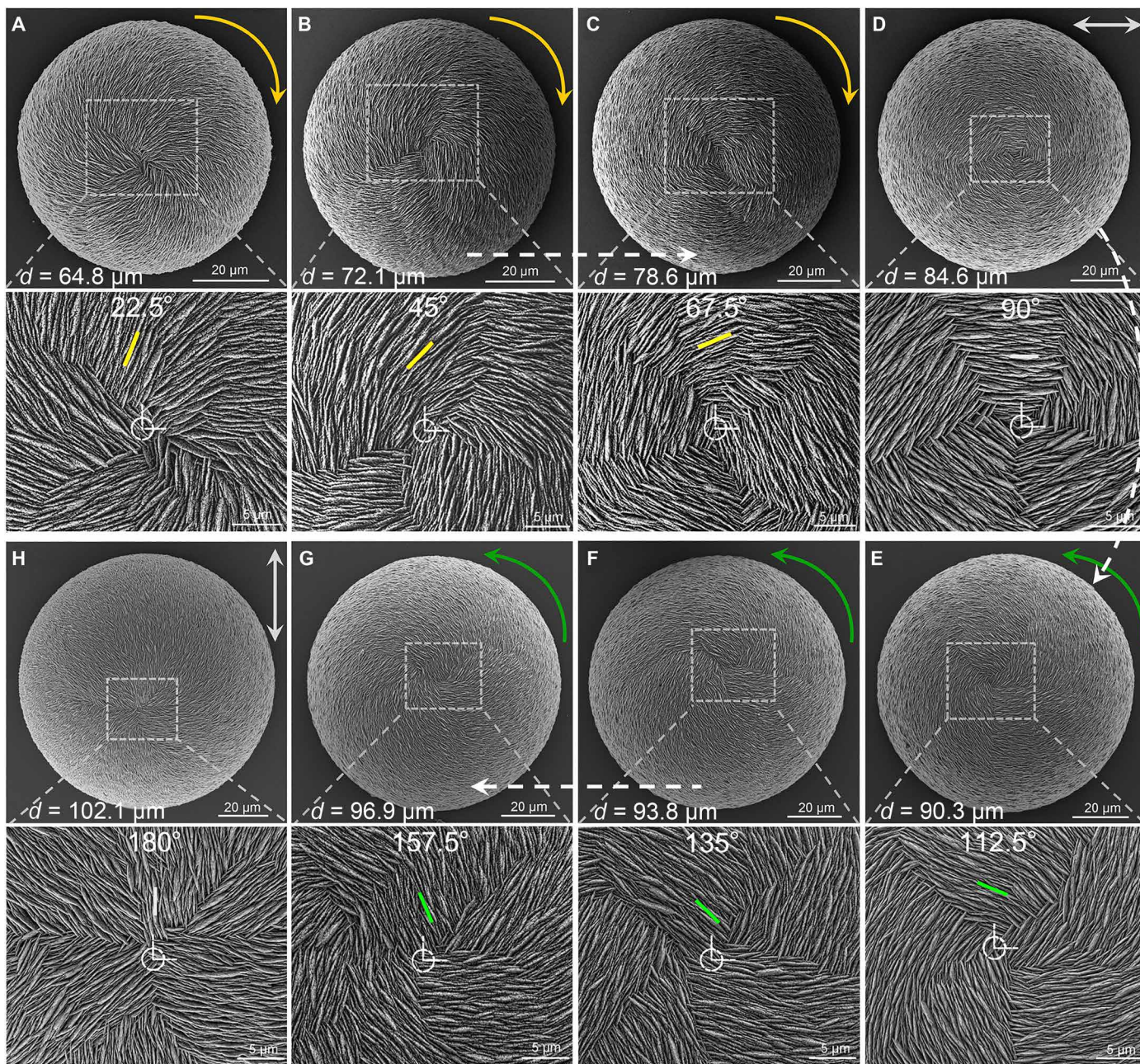
Fig. 5. Chiral switching by vertical platelet layer-by-layer rotation correlates with increasing size of vaterite helicoids during growth evolution in the presence of L-Asp. (**A** to **C**) SEM images at low (top) and corresponding high (bottom) magnification of clockwise (yellow arrows) vaterite helicoids during their growth evolution extending from the first transitional straight-radiating (0° reference start point) achiral vaterite helicoid as depicted previously in Fig.4D. As helicoids grow and increase in size, vertical platelets then successively rotate by 22.5° in the clockwise direction in each layer to reach first 22.5°, then 45°, then 67.5° relative to the start point (small yellow bars). (**D**) When the vertical platelets in the uppermost layer continue to rotate clockwise to the horizontal position (90° from the reference start point), the helicoid becomes achiral having the horizontal-surrounding platelet orientation (gray double-headed arrow and bar). (**E** to **G**) With further clockwise rotational growth (to reach first 112.5°, then 135°, and then 157.5°; green bars), helicoids have a counterclockwise chiral structure (green arrows). (**H**) Finally with additional growth, a transitional achiral state of the helicoid (180°) again appears (gray double-headed arrow, gray bar), completing a cycle to again form an achiral structure with the same morphology as that of the original straight-radiating platelet orientation (0°) of achiral helicoids (as shown earlier in Fig.4D), but now having a much larger size attributable to the additional growth by platelet layer additions.

(fig. S5), beyond the inclined-platelet region, four sequential vertical and rotated-platelet layers were observed in a very large helicoid ("2 to 5" in fig. S5A), which is consistent with that predicted from an achiral transitional helicoid having horizontal-surrounding vertical platelet orientation as shown in Fig. 5D, composed of four rotated-platelet layers. High-magnification SEM (including backscattered electron imaging) of five sequential platelet layers in the uppermost inclined-platelet region and the rotated-platelet region shows the

transition from sharp, on-edge views of platelets (fig. S5B1) toward more diffuse, blurred density images as the platelets rotate to the en face view (fig. S5B5) in the outermost layer 5.

The rotation between mother platelets (Fig. 6A, blue) and consequential daughter platelets (Fig. 6A, purple) between two adjacent layers was clearly identified at the surface of a nearly symmetric, straight-radiating platelet transitional achiral helicoid, and the measured rotation angle was 22.5° with the clockwise orientation, as expected for the L-Asp condition (Fig. 6A). Given that nanostructured chiral platelets are composed of subunit nanohexagonal prisms (nanoparticles, Fig. 2F) (19), it is reasonable to consider that this vertical platelet rotation structure should occur at the level of the subunit growth particle—between two nanoparticles—with one belonging to the mother platelet and the other to the daughter platelet in two successive platelet layers, respectively. To understand this stereo-specificity, using the sampling tools available in RosettaSurface (45), we explored potential geometries for two parallel vaterite slabs both with and without the addition of a monolayer of Asp between the slabs. In the absence of amino acid additives, besides the obvious most stable configuration of the mother and daughter nanoparticles being in perfect alignment at 0°, we located a structure with a reasonable lattice alignment at ~27° rotation. At this degree of rotation, a positively charged line of calcium atoms at the exposed surface of the mother vaterite aligned with a negatively charged line of carbonates at the exposed surface of the daughter vaterite over the length scale of the nanohexagon (fig. S6, A and B). This arrangement is consistent with adjacent nanoparticle rotation energy minimums seen also for rutile TiO_2 (46). However, in the vaterite system, in the presence of an added acidic L-Asp layer, the negatively charged L-Asp on the mother vaterite repels the negatively charged daughter vaterite surface. Furthermore, the local alignment of amino acids when the slabs are rotated ~27° in the clockwise direction shows reduced stability of the system (fig. S6, C to E). To obtain a better geometric match, we searched for plausible structures with a 22.5° clockwise rotation, as observed experimentally between two vertical platelet layers in chiral vaterite helicoids in the presence of L-Asp (Figs. 5 and 6A, and fig. S5). By searching both vertical and horizontal translations (see Materials and Methods), we identified a candidate model with a 22.5° clockwise rotation between the vaterite slabs that positions the negatively charged carboxyl groups facing away from the mother surface to minimize repulsion with the negatively charged carbonate ions of the daughter surface (Fig. 6, B and C, and fig. S6). This layer-by-layer rotation growth mechanism between vertical platelet layers would induce the chiral switch of vaterite helicoids in their growth evolution process (Fig. 6, D to F).

We thus summarize a cyclic mechanistic model for chiral vaterite helicoid growth which results in the switching of helicoid chirality. This chiral switch cycle can be partitioned into four successive steps (here reflecting the effects of L-Asp): (i) an achiral straight-radiating vertical platelet start point at 0°; (ii) a first clockwise platelet rotational step of 22.5°, which repeats in subsequent growth layers to reach 45° and then 67.5° from the start point, resulting in a clockwise chiral helicoid; (iii) a transitional horizontal-surrounding platelet orientation step that occurs at 90° from the start point, resulting in an achiral helicoid; and (iv) continued 22.5° clockwise platelet rotations to reach 112.5°, 135°, and 157.5° from the start point, resulting in a counterclockwise chiral helicoid (Fig. 6, D to F, and movie S1). This chiral switch cycle is completely consistent with the chiral switch

process observed for very large vaterite helicoids observed by SEM (Fig. 5). Furthermore, this chiral switch cycle also implies that similar successional four-step growth of vaterite helicoids should continue to repeat via this rotation mechanism, with continued growth producing ever-increasing sizes compared to a single cycle alone as shown in Fig. 5. Evidence of this amplified growth was successfully observed by SEM in subsequent additional growth cycles (fig. S7). These observations are consistent with our rotation growth model for the chiral switching of the vaterite helicoids in the presence of a single enantiomer of amino acid.

Potential general strategy in biology

This layer-by-layer rotational circular growth model for vaterite structures, which also provides a chiral switching mechanism, may be part of organic contributions to chiral switches observed in mineralized structures in biology, where biomineralized shells and other structures such as coccolith skeletons and pathologic human vaterite otoconia have chiral structures. Not only do the data support the postulate that simple acidic amino acids are potentially involved in producing chiral mineralized architectures both large and small, but they also additionally suggest that more complex chiral biomolecules may provide additional hierarchical instructions for extended structure in biomineralization. For example, for the small calcium carbonate structures of coccolith skeletons which are composed of discrete platelet-based, disc-shaped elements having periodically alternating (cycling) configurations, and for the larger hierarchically organized entire skeletons of coccoliths, these factors may be at play. Continuing this notion, it can be readily considered that their three different architectural forms (being left-handed, symmetrical achiral, and right-handed, or a combination thereof), and their spatial arrangements, could respectively correspond to the relative growth regions/stages we have described here for a layer-by-layer rotation and circular growth model (Fig. 6 and movie S1) (9–11). Furthermore, the model includes the possibility for coexistence of different chiral orientations in adjacent circular layers, as can occur in coccolith skeletons, with a repeating rotation angle between the layers (Fig. 1A and fig. S8) (9). On the basis of the remarkable similarity between our rounded chiral synthetic structures and rounded chiral human pathologic otoconia retrieved from the inner ear [as presented by Wright et al. (29)] (Fig. 1, B and C), it seems likely that other otoconial vaterite forms could be found having any of the additional three forms that our model predicts from observations of a simplified synthetic system (fig. S9).

CONCLUSION

In summary, this work demonstrates that two imperfect oriented attachment growth mechanisms operate in establishing chiral hierarchical vaterite helicoids induced by the adsorption of a single chiral enantiomer of an acidic amino acid onto a vaterite crystal, and whose helicoid chirality can be switched. These findings advance our understanding of why, despite a lack of D-enantiomer amino acids in biology—the "Achilles heel" of understanding the origin of enantiomeric pairs of biominerals from chiral amino acids—various enantiomorphs of biomineral may indeed be formed by homochiral biomolecules (more specifically L-acidic amino acids, as found in nature). The findings also describe a new organizational function involving mineral crystal-biomolecule interactions over different length scales that may prove useful in the development of novel composite/hybrid functional
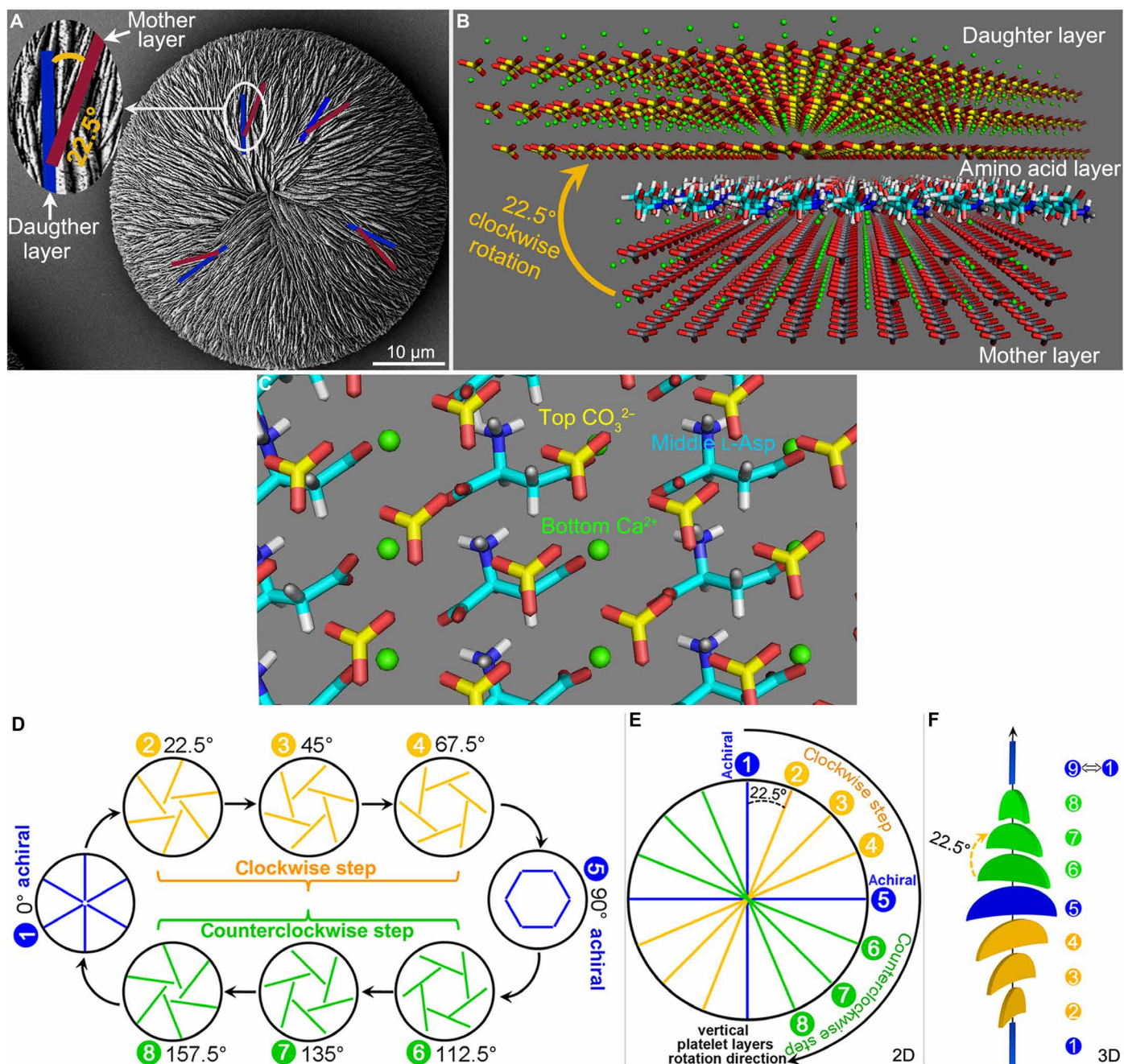
Fig. 6. Mechanism leading to chiral switching as induced by chiral amino acid enantiomer. (**A**) SEM image of a nearly achiral vaterite helicoid showing the clockwise rotation of 22.5° between two connected vertical platelets in adjacent mother (blue) and daughter (purple) layers in the rotated-platelet region. (**B**) A model at the (100) plane for two adjacent vertical and rotated vaterite platelet layers showing details of a consequential rotated daughter vertical platelet position relative to the mother vertical platelet position, with intervening amino acid layer, as identified by RosettaSurface computational simulation fixing the clockwise rotation at 22.5°. Vaterite crystal atoms: Ca, green; C, gray in mother layer and yellow in daughter layer; O, red. (**C**) High-resolution simplified image showing the configuration at the 22.5° rotation between the bottom mother vaterite layer with exposed surface calcium (green), the intervening middle L-Asp layer (blue), and the top daughter vaterite layer with exposed surface carbonates (yellow). (**D**) Schematic summary (of a top view) of the chiral switching of surface structures in vaterite helicoids caused by the 22.5° layer-by-layer clockwise rotation in the presence of the L-enantiomer of Asp, whose replication/amplification with further growth leads to the 180° chiral switch cycle. The entire cycle is composed of four steps with eight continuous 22.5° clockwise-rotated layers: (i) an achiral straight-radiating vertical platelet start point at 0°; (ii) a first clockwise platelet rotational step of 22.5°, which repeats in subsequent growth layers to reach 45°, and then 67.5° from the start point resulting in a clockwise chiral helicoid; (iii) a transitional horizontal-surrounding platelet orientation step that occurs at 90° from the start point, resulting in an achiral helicoid; and (iv) continued 22.5° clockwise platelet rotations to reach 112.5°, then 135°, and then 157.5° from the start point, resulting in a counterclockwise chiral helicoid. (**E** and **F**) Two-dimensional (2D) (top view) and 3D (side view) schematics of the relationship at one location for one chiral switching cycle of eight successive clockwise rotations of 22.5° of vertical platelet layer configurations, and the chiral status of the corresponding whole vaterite helicoids, as produced in the presence of the L-enantiomer of Asp.

materials. The findings also allowed us to build a growth model for pathologic human inner ear otoconia that predicts other pathologic forms—as yet to be discovered—whose formation may one day be modified by therapies based on this understanding.

MATERIALS AND METHODS
Materials
Calcium chloride ($CaCl_2$), sodium carbonate (Na_2CO_3), and aspartic acid and the other chemicals used in this study were purchased from Fisher Scientific and Sigma-Aldrich, respectively. All solutions were prepared using triple distilled water.

Calcium carbonate growth method
The method of obtaining calcium carbonate in the presence of single chiral enantiomer of amino acid was described in our previous work with minor change (19). Briefly, in a 250-ml covered beaker, calcium carbonate was obtained by adding 50 ml of 3 mM Na_2CO_3 to 50 ml of 3 mM $CaCl_2$ (Fisher Scientific) solution containing 40 mM acidic amino acid (Sigma-Aldrich), and then the solution pH was adjusted to 10.5 ± 0.2 by stepwise addition of 1 M NaOH at 20°C. Final concentrations of $CaCl_2$, Na_2CO_3, and chiral acidic amino acids were 1.5, 1.5, and 20 mM, respectively. The solution was maintained at room temperature during the entire growth period, and no stirring was performed at any time. When particulate material began to appear at the bottom of the beaker (as observed by optical microscopy occurring between 12 and 24 hours, and not in solution), round glass coverslips (to facilitate removal and subsequent mineral analysis) were gently dropped to the bottom of the beaker. To keep continuous vaterite growth under supersaturation conditions, the growth solution was replaced at 5-day intervals with fresh, sterile calcium carbonate solution with chiral Asp enantiomer (at pH 10.5); without growth solution changes, all calcium carbonate growth processes were similar, but slower. Periodically, after different reaction times, glass coverslips with attached calcium carbonate particles (helicoids) were removed from the beaker and washed gently with triple distilled water and ethanol, and then allowed to dry in a vacuum desiccator at room temperature before analysis.

Sample characterization
Scanning electronic microscopy
To improve sample conductivity, we coated specimens for imaging by SEM with a 2-nm electrically conductive layer of Pt using a Leica Microsystems EM ACE600 sputter coater, followed by imaging at high vacuum using a FEI Quanta 450 FE-ESEM (FEI Company), operating at a voltage of 5 kV, and equipped with an Everhart-Thornley secondary electron detector.

For ultrastructural characterization of cross-sectioned vaterite helicoids by SEM, the glass coverslips with grown calcium carbonate helicoids were embedded in LR White acrylic resin or epoxy resin (Electron Microscopy Sciences). After polymerization of the resins, cross sections of vaterite helicoids were obtained by a series of fine-grit polishing steps. First, a 3000-grit water stone (Lee Valley Company) was used to remove the outer resin, and this was then followed by the use of a 0.2-μm colloidal silica solution on a Struers MD Chem cloth to finely polish vaterite helicoids for 10 min. To remove aggregated silica from the samples, sonication in triple distilled water was performed. The polished samples were stored in a vacuum desiccator prior to viewing by SEM.

Focused-ion beam scanning electron microscopy
To detect the inner structure and height changes in vaterite helicoids having different chiralities (clockwise or counterclockwise direction) or different symmetries (achiral transitional straight-radiating or horizontal-surrounding platelet orientation), we also prepared SEM samples of cross sections of helicoids using a Helios NanoLab 660 DualBeam (FEI Company) using conventional FIB techniques. All samples were coated with 3-nm platinum layer to enhance electrical conductivity. To prevent ion beam damages on the surface of helicoids during the process of FIB milling, we deposited a protective layer of platinum (2-μm thickness) onto the specimen surface in the selected area. Material surrounding the region of interest was removed using a 30-kV ion beam and a current ranging from 65 to 2.5 nA. To exclude a perfectly flat surface resulting from FIB cutting and milling, and to allow for some topography to be visualized, the samples were briefly etched with phosphoric acid (pH 4) 3 × 20 s, then were rinsed with triple distilled water and ethanol, and allowed to dry in a vacuum desiccator at room temperature before SEM investigation.

Computational simulation
We used PyMOL (PyMOL Molecular Graphics System, version 1.8; Schrödinger LLC) and PyRosetta (47), in conjunction with modules from RosettaSurface (45), to sample potential geometries for two parallel vaterite (100) slabs with and without a monolayer of amino acids adsorbed on the mother slab. The goal of our modeling was to propose a plausible geometrical model for the core nanoparticle interface at the observed 22.5° oriented preference between the two vertical mother and daughter platelet layers in the presence of Asp.

Chiral acidic amino acid models. We constructed L-Asp with ideal bond lengths and angles (48). The individual amino acids were represented as zwitterions with charged amino and carboxyl termini.

Vaterite (100) model. We constructed a pair of parallel vaterite (100) slabs using CrystalMaker version 9 and vaterite unit cell coordinates from Kamhi (49). The thickness of the slabs (1.2 nm) was chosen to exceed the maximum interaction distance in the Rosetta energy function, and the length and width (10 × 10 nm) were chosen to match the observed size of the nanohexagons. A pristine, neutrally charged termination was used for the vaterite surface as described in our previous work (19).

Simulation of bare vaterite surfaces. We optimized the distance between two facing parallel vaterite (100) slabs by energy minimization and rotated the top surface around the center of the bottom surface at 0.5° intervals. One local minimum energy structure at 27° rotation is shown in fig. S6.

Simulation of vaterite surfaces interacting with 22.5° rotation with monolayer of L-Asp. To generate an initial configuration for the system, we began with a low-energy structure of L-Asp adsorbed on one vaterite (100) surface, determined in previous work (19). We then applied translational symmetry operators to produce a 9 × 9 unit cell monolayer grid of L-Asp adsorbed onto the face of the mother slab.

Search algorithm. The degrees of freedom sampled by our algorithm include (i) translation between the two parallel slabs and (ii) the z distance (height) between the two parallel slabs. To determine a plausible structure with a 22.5° rotation between the mother and daughter slabs, we first manually rotated the slabs to a 22.5° relative rotation. We then sampled all possible translations between the two slabs in 0.1 Å increments using a grid search. Amino acid conformation was fixed. We selected the translation that minimized the energy for a 22.5° rotation as our proposed geometrical model.

Energy function. We used Raitieri *et al.*'s calcium carbonate parameters (*50*), in combination with the Rosetta Talaris-2013 energy function (*51*). Raitieri *et al.*'s function includes van der Waals radii and partial charges of the mineral, and it has been used for molecular adsorption, nucleation, and surface morphologies. The Rosetta Talaris-2013 function includes a combination of terms for van der Waals energies, hydrogen bonds, electrostatics, and solvation via an implicit solvent Gaussian exclusion model (*52*), and it has been validated and used for biomolecular structure prediction and design. To eliminate edge effects, we only considered pairwise interactions between atoms in the "core" region of the system (defined as a 10 Å sphere centered on the central Asp monomer in the 9×9 grid, roughly covering about nine unit cells).

SUPPLEMENTARY MATERIALS

Supplementary material for this article is available at http://advances.sciencemag.org/cgi/content/full/4/8/eaas9819/DC1

Supplementary Text

Fig. S1. Growth of hierarchically organized vaterite suprastructures stabilized by amino acids.
Fig. S2. Chiral switching of hierarchically organized vaterite helicoid suprastructures in the presence of single chiral D-enantiomer of amino acid (D-Asp).
Fig. S3. Size-related uniformity among vaterite helicoids having chiral switching when grown in the presence of a single chiral enantiomer of amino acid (D-Asp) at low supersaturation conditions.
Fig. S4. Growth evolution of hierarchically organized vaterite helicoids with respect to size and height.
Fig. S5. Multilayering within chiral vaterite helicoids.
Fig. S6. Instability of adjacent rotated vertical vaterite platelets caused by the addition of chiral amino acid enantiomer.
Fig. S7. Chiral switching by platelet layer-by-layer rotation correlates with size/growth of very large helicoids.
Fig. S8. Layer-by-layer growth models as a potential general strategy for switching chiral structures as observed in biology.
Fig. S9. Prediction of three as-yet unfound forms of human pathologic vaterite otoconia based on the vaterite helicoid chiral switching growth model.
Movie S1. Animation showing chiral switching in vaterite helicoidal suprastructures occurring by a vertical platelet layer-by-layer rotation mechanism in the presence of a single chiral enantiomer of acidic amino acid.
Reference (*53*)

REFERENCES AND NOTES

1. J. J. De Yoreo, P. U. P. A. Gilbert, N. A. J. M. Sommerdijk, R. L. Penn, S. Whitelam, D. Joester, H. Zhang, J. D. Rimer, A. Navrotsky, J. F. Banfield, A. F. Wallace, F. M. Michel, F. C. Meldrum, H. Cölfen, P. M. Dove, Crystallization by particle attachment in synthetic, biogenic, and geologic environments. *Science* **349**, aaa6760 (2015).
2. C. Grand, N. H. Patel, Nodal signalling is involved in left–right asymmetry in snails. *Nature* **457**, 1007–1011 (2009).
3. R. Ueshima, T. Asami, Evolution: Single-gene speciation by left–right reversal. *Nature* **425**, 679 (2003).
4. M. Schilthuizen, A. Davison, The convoluted evolution of snail chirality. *Naturwissenschaften* **92**, 504–515 (2005).
5. C. Sutcharit, T. Asami, S. Panha, Evolution of whole-body enantiomorphy in the tree snail genus *Amphidromus*. *J. Evol. Biol.* **20**, 661–672 (2007).
6. L. Bozzetti, Description of a new species of the genus *Comitas* from north eastern Somalia (Gastropoda Turridae). *Bull. Inst. Malac. Tokyo* **3**, 33–35 (1994).
7. L. Addadi, S. Weiner, Biomineralization: Crystals, asymmetry and life. *Nature* **411**, 753–755 (2001).
8. O. J. Bandy, Geologic significance of coiling ratios in the foraminifer *Globigerina pachyderma* (Ehrenberg). *J. Paleontol.* **34**, 671–681 (1960).
9. J. R. Young, K. Henriksen, Biomineralization wihin vesicles: The calcite of coccoliths. *Rev. Mineral. Geochem.* **54**, 189–215 (2003).
10. G. M. Durak, A. R. Taylor, C. E. Walker, I. Probert, C. de Vargas, S. Audic, D. Schroeder, C. Brownlee, G. L. Wheeler, A role for diatom-like silicon transporters in calcifying coccolithophores. *Nat. Commun.* **7**, 10543 (2016).
11. P. R. Brown, Calcareous nannofossils from the Paleocene/Eocene Thermal Maximum interval of southern Tanzania (TDP Site 14). *J. Nannoplankt. Res.* **31**, 11–38 (2010).
12. S. M. Morrow, A. J. Bissette, S. P. Fletcher, Transmission of chirality through space and across length scales. *Nat. Nanotechnol.* **12**, 410–419 (2017).
13. W. Feng, J.-Y. Kim, X. Wang, H. A. Calcaterra, Z. Qu, L. Meshi, N. A. Kotov, Assembly of mesoscale helices with near-unity enantiomeric excess and light-matter interactions for chiral semiconductors. *Sci. Adv.* **3**, e1601159 (2017).
14. S. Che, Z. Liu, T. Ohsuna, K. Sakamoto, O. Terasaki, T. Tatsumi, Synthesis and characterization of chiral mesoporous silica. *Nature* **429**, 281–284 (2004).
15. S. Jiang, M. Chekini, Z.-B. Qu, Y. Wang, A. Yeltik, Y. Liu, A. Kotlyar, T. Zhang, B. Li, H. V. Demir, N. A. Kotov, Chiral ceramic nanoparticles and peptide catalysis. *J. Am. Chem. Soc.* **139**, 13701–13712 (2017).
16. C. A. Orme, A. Noy, A. Wierzbicki, M. T. McBride, M. Grantham, H. H. Teng, P. M. Dove, J. J. DeYoreo, Formation of chiral morphologies through selective binding of amino acids to calcite surface steps. *Nature* **411**, 775–779 (2001).
17. L. A. Gower, D. A. Tirrell, Calcium carbonate films and helices grown in solutions of poly(aspartate). *J. Cryst. Growth* **191**, 153–160 (1998).
18. T. Sugawara, Y. Suwa, K. Ohkawa, H. Yamamoto, Chiral biomineralization: Mirror-imaged helical growth of calcite with chiral phosphoserine copolypeptides. *Macromol. Rapid Commun.* **24**, 847–851 (2003).
19. W. Jiang, M. S. Pacella, D. Athanasiadou, V. Nelea, H. Vali, R. M. Hazen, J. J. Gray, M. D. McKee, Chiral acidic amino acids induce chiral hierarchical structure in calcium carbonate. *Nat. Commun.* **8**, 15066 (2017).
20. R. M. Hazen, D. S. Sholl, Chiral selection on inorganic crystalline surfaces. *Nat. Mater.* **2**, 367–374 (2003).
21. W. Jiang, H. Pan, Z. Zhang, S. R. Qiu, J. D. Kim, X. Xu, R. Tang, Switchable chiral selection of aspartic acids by dynamic states of brushite. *J. Am. Chem. Soc.* **139**, 8562–8569 (2017).
22. L. Addadi, S. Weiner, Interactions between acidic proteins and crystals: Stereochemical requirements in biomineralization. *Proc. Natl. Acad. Sci. U.S.A.* **82**, 4110–4114 (1985).
23. A. Gal, R. Wirth, J. Kopka, P. Fratzl, D. Faivre, A. Scheffel, Macromolecular recognition directs calcium ions to coccolith mineralization sites. *Science* **353**, 590–593 (2016).
24. K. T. Moreland, M. Hong, W. Lu, C. W. Rowley, D. M. Ornitz, J. J. De Yoreo, R. Thalmann, In vitro calcite crystal morphology is modulated by otoconial proteins otolin-1 and otoconin-90. *PLOS ONE* **9**, e95333 (2014).
25. E. Verpy, M. Leibovici, C. Petit, Characterization of otoconin-95, the major protein of murine otoconia, provides insights into the formation of these inner ear biominerals. *Proc. Natl. Acad. Sci. U.S.A.* **96**, 529–534 (1999).
26. C. Söllner, M. Burghammer, E. Busch-Nentwich, J. Berger, H. Schwarz, C. Riekel, T. Nicolson, Control of crystal size and lattice formation by starmaker in otolith biomineralization. *Science* **302**, 28–286 (2003).
27. S. L. Miller, A production of amino acids under possible primitive earth conditions. *Science* **117**, 528–529 (1953).
28. S. W. Fox, How did life begin? *Science* **132**, 200–208 (1960).
29. C. G. Wright, R. C. Rouse, G. H. Zajic, S. D. Schaefer, D. G. Hubbard, L. A. Barnard, A calcareous concretion in the posterior semicircular duct of a human labyrinth. *Am. J. Otolaryngol.* **3**, 196–201 (1982).
30. D. J. Sutor, S. E. Wooley, Gallstone of unusual composition: Calcite, aragonite and vaterite. *Science* **159**, 1113–1114 (1968).
31. J. Kanakis, P. Malkaj, J. Petroheilos, E. Dalas, The crystallization of calcium carbonate on porcine and human cardiac valves and the antimineralization effect of sodium alginate. *J. Cryst. Growth* **223**, 557–564 (2001).
32. B. Hasse, H. Ehrenberg, J. C. Marxen, W. Becker, M. Epple, Calcium carbonate modifications in the mineralized shell of the freshwater snail *Biomphalariaglabrata*. *Chem. Eur. J.* **6**, 3679–3685 (2000).
33. L. Kabalah-Amitai, B. Mayzel, Y. Kauffmann, A. N. Fitch, L. Bloch, P. U. P. A. Gilbert, B. Pokroy, Vaterite crystals contain two interspersed crystal structures. *Science* **340**, 454–457 (2013).
34. D. E. Jacob, R. Wirth, O. B. A. Agbaje, O. Branson, S. M. Eggins, Planktic foraminifera form their shells via metastable carbonate phases. *Nat. Commun.* **8**, 1265 (2017).
35. C. G. Wright, R. C. Rouse, L.-G. Johnsson, A. G. Weinberg, D. G. Hubbard, Vaterite otoconia in two cases of otoconial membrane dysplasia. *Ann. Otol. Rhinol. Laryngol.* **91** (Pt. 1), 193–199 (1982).
36. R. W. Sattin, Falls among older persons: A public health perspective. *Annu. Rev. Public Health* **13**, 489–508 (1992).
37. R. L. Penn, J. F. Banfield, Imperfect oriented attachment: Dislocation generation in defect-free nanocrystals. *Science* **281**, 969–971 (1998).
38. M. H. Nielsen, S. Aloni, J. J. De Yoreo, In situ TEM imaging of $CaCO_3$ nucleation reveals coexistence of direct and indirect pathways. *Science* **345**, 1158–1162 (2014).
39. A. G. Shtukenberg, Y. O. Punin, A. Gujral, B. Kahr, Growth actuated bending and twisting of single crystals. *Angew. Chem. Int. Ed.* **53**, 672–699 (2014).
40. M. O. Lorenzo, C. J. Baddeley, C. Muryn, R. Raval, Extended surface chirality from supramolecular assemblies of adsorbed chiral molecules. *Nature* **404**, 376–379 (2000).
41. S. Jana, M. de Frutos, P. Davidson, B. Abécassis, Ligand-induced twisting of nanoplatelets and their self-assembly into chiral ribbons. *Sci. Adv.* **3**, e1701483 (2017).
42. F. Bertolotti, D. N. Dirin, M. Ibáñez, F. Krumeich, A. Cervellino, R. Frison, O. Voznyy, E. H. Sargent, M. V. Kovalenko, A. Guagliardi, N. Masciocchi, Crystal symmetry breaking

and vacancies in colloidal lead chalcogenide quantum dots. *Nat. Mater.* **15**, 987–994 (2016).

43. V Sharma, M Crne, J. O. Park, M Srinivasarao, Structural origin of circularly polarized iridescence in jeweled beetles. *Science* **325**, 449–451 (2009).

44. K. E. Shopsowitz, H. Qi, W. Y. Hamad, M. J. MacLachlan, Free-standing mesoporous silica films with tunable chiral nematic structures. *Nature* **468**, 422–425 (2010).

45. M. S. Pacella, C. E. Koo da, R. A. Thottungal, J. J. Gray, Using the RosettaSurface algorithm to predict protein structure at mineral surfaces. *Methods Enzymol.* **532**, 343–566 (2013).

46. X. Zhang, Y. He, M. L. Sushko, J. Liu, L. Luo, J. J. De Yoreo, S. X. Mao, C. Wang, K. M. Rosso, Direction-specific van der Waals attraction between rutile TiO₂ nanocrystals. *Science* **365**, 434–437 (2017).

47. S. Chaudhury, S. Lyskov, J. J. Gray, PyRosetta: A script-based interface for implementing molecular modeling algorithms using Rosetta. *Bioinformatics* **26**, 689–691 (2010).

48. R. A. Engh, R. Huber, Accurate bond and angle parameters for X-ray protein structure refinement. *Acta Crystallogr. A* **47**, 392–400 (1991).

49. S. Kamhi, On the structure of vaterite CaCO3. *Acta Crystallogr.* **16**, 770–772 (1963).

50. P. Raiteri, J. D. Gale, D. Quigley, P. M. Rodger, Derivation of an accurate force-field for simulating the growth of calcium carbonate from aqueous solution: A new model for the calcite–water interface. *J. Phys. Chem. C* **114**, 5997–6010 (2010).

51. M. J. O'Meara, A. Leaver-Fay, M. D. Tyka, A. Stein, K. Houlihan, F. DiMaio, P. Bradley, T. Kortemme, D. Baker, J. Snoeyink, B. Kuhlman, Combined covalent-electrostatic model of hydrogen bonding improves structure prediction with Rosetta. *J. Chem. Theory Comput.* **11**, 609–622 (2015).

52. T. Lazaridis, M. Karplus, Effective energy function for proteins in solution. *Proteins* **35**, 133–152 (1999).

53. J. J. De Yoreo, P. G. Vekilov, Principles of crystal nucleation and growth. *Rev. Mineral. Geochem.* **54**, 57–93 (2003).

Citation: W. Jiang, M. S. Pacella, H. Vali, J. J. Gray, M. D. McKee, Chiral switching in biomineral suprastructures induced by homochiral L-amino acid. *Sci. Adv.* **4**, eaas9819 (2018).